Elastic constants, internal friction, and piezoelectric coefficient of α-TeO_2

Hirotsugu Ogi, Masashi Fukunaga, and Masahiko Hirao
Graduate School of Engineering Science, Osaka University, Machikaneyama 1-3, Toyonaka, Osaka 560-8531, Japan

Hassel Ledbetter
Los Alamos National Laboratory, M/S E536, Los Alamos, New Mexico 87545, USA

(Received 7 August 2003; revised manuscript received 2 October 2003; published 15 January 2004)

We studied the interrelationship of elastic and piezoelectric properties with the lattice structure and crystal physics of paratellurite (α-TeO_2). Tetragonal paratellurite (D_4^4,$P422$) shows six independent elastic constants C_{ijkl}, the associated internal friction Q_{ijkl}^{-1}, and one piezoelectric coefficient e_{14}. We determined simultaneously these material coefficients using resonant ultrasound spectroscopy coupled with laser-Doppler interferometry. Mode identification, essential for success, was done by measuring the displacement distributions on a vibrating-specimen surface. Our C_{ijkl} were consistent with reported values measured by conventional methods. Our e_{14} exceeds the reported value by 53%. We focus on several unusual elastic properties, including a negative Poisson ratio. Considering a star-shape truss structure on the basal plane consistently explains all of them. Internal friction correlates with the C_{ijkl} temperature derivatives, suggesting phonon-phonon interactions as a dominant cause of the mechanical loss.

DOI: 10.1103/PhysRevB.69.024104 PACS number(s): 62.20.Dc, 43.35.+d, 62.40.+i, 77.65.Bn

I. INTRODUCTION

Paratellurite (α-TeO_2) finds wide use in many advanced devices because of its outstanding acousto-optical, dielectric, and electro-optic properties.[1,2] Its crystallographic structure received intensive study by many researchers.[3–8] Paratellurite belongs to crystals with 422 point-group symmetry (tetragonal) and shows six independent elastic-stiffness coefficients C_{ijkl}, corresponding six internal frictions Q_{ijkl}^{-1}, one piezoelectric coefficient e_{14}, and two dielectric coefficients ε_{ij}. Their accurate measurement is of great importance both for scientific and practical studies. Elastic constants, for example, reflect crystal structure and interatomic-bond strength. They are indispensable for designing surface-acoustic-wave (SAW) and acousto-optic devices. The present study contains two principal purposes. First, determine all the material coefficients accurately on a single monocrystal using a new acoustic-spectroscopic method. Second, clarify paratellurite's remarkable elastic properties.

Crystal-system design often requires a complete set of the material coefficients. The dielectric coefficients are available accurately from low-frequency capacitance measurements,[9] but measuring all of the elastic and piezoelectric coefficients presents a formidable task with conventional methods[9,10] because they involve many independent measurements on many crystals in many orientations: pulse-echo measurements or rod-resonance measurements coupled with the resonance-antiresonance measurements of electric impedance. One must solve a set of labyrinthine equations to deduce the C_{ijkl} and e_{ijk}. Various errors easily occur, associated with use of different methods and different crystals, crystal misorientation, resonance-frequency shifts by attaching electrodes and acoustic transducers, and so on. Here, we describe an advanced methodology that yields all the elastic, anelastic, and piezoelectric coefficients from a single rectangular-parallelepiped specimen. The mechanical resonance frequencies of a piezoelectric solid depend on the C_{ijkl} and e_{ijk}. Resonant ultrasound spectroscopy (RUS) can detect them, from which an inverse calculation yields the needed coefficients. Previously, this approach was used to determine the C_{ijkl} of solids.[11–15] Schreuer[16] applied the RUS method to piezoelectric crystals to deduce the C_{ijkl} and e_{ijk}. However, the mode-identification problem remains. To deduce the e_{ijk} along with C_{ijkl}, resonance-frequency measurements must be done with a sufficiently high accuracy because contributions of e_{ijk} to resonance frequencies are usually much smaller than those of C_{ijkl}. Even more important is mode matching between observed and calculated resonances. Mode mismatch is fatal to obtaining these less-contributing coefficients. Therefore, obtaining reliable e_{ijk} and C_{ijkl} by the RUS method requires precise frequency measurement and correct mode identification. We overcame these difficulties by developing a piezoelectric tripod to detect *free* oscillation of a specimen and by incorporating laser-Doppler interferometry into the resonance measurement to measure the surface displacements for identifying the vibrating modes. For the internal-friction tensor Q_{ijkl}^{-1}, we deduced them from peak widths of individual resonances.

Remarkable elastic anisotropy of paratellurite was reported by several researchers.[3–8] They attributed it to the strong and weak Te-O-bond stretching. However, they did not discuss other important and unusual properties such as a negative Poisson ratio for a deformation along a $\langle 110 \rangle$ direction. We show that the conventional interpretation considering only bond stretching fails to explain the elastic properties, and we propose a weak-bond-bending model with a star-shape truss structure. We measure all of the internal-friction components and find a correlation between internal friction and elastic-constant temperature derivatives. This correlation suggests phonon-phonon interactions.

II. MATERIAL

We used an oriented rectangular-parallelepiped monocrystal of paratellurite, measuring 6.778 mm by 7.022 mm by

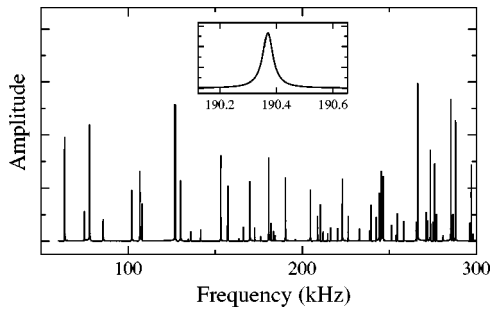

FIG. 1. Resonance spectrum of the paratellurite monocrystal.

8.963 mm. Laue x-ray diffraction confirmed orientations within 0.2°. The three orthogonal faces were perpendicular to [100], [010], and [001] directions, along which we take the x_1, x_2, and x_3 axes, respectively. Using Archimedes's method and distilled water as a standard, we found a mass density $\rho = 5984\ \mathrm{kg/m^3}$. For 422-symmetry materials, the coefficients take the form in contracted notation:

$$[C_{ij}] = \begin{bmatrix} C_{11} & C_{12} & C_{13} & 0 & 0 & 0 \\ C_{12} & C_{11} & C_{13} & 0 & 0 & 0 \\ C_{13} & C_{13} & C_{33} & 0 & 0 & 0 \\ 0 & 0 & 0 & C_{44} & 0 & 0 \\ 0 & 0 & 0 & 0 & C_{44} & 0 \\ 0 & 0 & 0 & 0 & 0 & C_{66} \end{bmatrix}, \quad (1)$$

$$[e_{ij}] = \begin{bmatrix} 0 & 0 & 0 & e_{14} & 0 & 0 \\ 0 & 0 & 0 & 0 & -e_{14} & 0 \\ 0 & 0 & 0 & 0 & 0 & 0 \end{bmatrix}, \quad (2)$$

and

$$[\varepsilon_{ij}] = \begin{bmatrix} \varepsilon_{11} & 0 & 0 \\ 0 & \varepsilon_{11} & 0 \\ 0 & 0 & \varepsilon_{33} \end{bmatrix}. \quad (3)$$

Besides, there are six independent internal frictions Q^{-1}_{ijkl}, which indicate the ratios of imaginary-to-real parts of the complex elastic stiffnesses $\tilde{C}_{ijkl}$:[13]

$$\tilde{C}_{ijkl} = C_{ijkl}(1 + jQ^{-1}_{ijkl}). \quad (4)$$

III. MEASUREMENT

A. RUS/laser technique

The piezoelectric tripod consists of two pinducers for generation and detection of vibration, and one needle just for support. Because no external force was applied to the specimen, except for specimen weight, and no coupling agent was used, the acoustical coupling between the pinducers and specimen remains stable and ideal *free* vibrations occur. A frequency scan detected all the resonance peaks in a frequency band as shown in Fig. 1. Peak-width measurements yielded internal frictions of individual resonance modes. We measured the resonance frequencies and corresponding internal frictions at constant temperature $30 \pm 0.02\,^{\circ}\mathrm{C}$ in vacuum ($\sim 10^{-3}$ Torr). Thus, little energy leaks into the air, which otherwise would affect the internal-friction measurement as described below. Reproducibility among independent measurements was better than 10^{-5} for resonance frequencies.

After finishing the series of measurements, we deposited a 100-nm aluminum film on the surface perpendicular to the x_1 axis to measure distributions of the out-of-plane displacement for mode identification. This deposition was needed because paratellurite is transparent. The specimen surface was scanned with a He-Ne laser beam, detecting the out-of-plane displacements. Frequency shifts from the aluminum-film addition were so small (~0.01%) that the modes remained clearly identified after the deposition.

B. Inverse calculation

Resonance frequencies can be calculated from specimen's mass density, dimensions, and all the coefficients using Lagrangian minimization with the Rayleigh-Ritz method with a sufficient accuracy. Such a forward calculation was established by Ohno.[17] He considered the weak form of the Lagrangian in a piezoelectric material:

$$L = \frac{1}{2}\int_V \left(S_{ij}C_{ijkl}S_{kl} - \frac{\partial \phi}{\partial x_m}\varepsilon_{mn}\frac{\partial \phi}{\partial x_n} + 2\frac{\partial \phi}{\partial x_m}e_{mkl}S_{kl} - \rho\omega^2 u_i u_i \right) dV. \quad (5)$$

Here u_i denotes the displacement along the x_i axis, S_{ij} a component of the strain tensor, ϕ the electric potential, ρ the mass density, and ω the angular frequency. The stationary point of the Lagrangian ($\delta L = 0$) gives the resonance modes. Because analytical solutions for the displacements and electric potential are unavailable, he approximated them with linear combinations of the basis functions ψ consisting of normalized Legendre polynomials:

$$u_i(x_1, x_2, x_3) = \sum_k a^i_k \Psi^i_k(x_1, x_2, x_3), \quad (6)$$

$$\phi(x_1, x_2, x_3) = \sum_k a^\phi_k \Psi^\phi_k(x_1, x_2, x_3). \quad (7)$$

Here

$$\Psi_k(x_1, x_2, x_3) = \sqrt{\frac{8}{L_1 L_2 L_3}}\,\overline{P}_l(2x_1/L_1)\overline{P}_m(2x_2/L_2)\overline{P}_n(2x_3/L_3). \quad (8)$$

$\overline{P}_l$ denotes the normalized Legendre polynomial of degree l, and L_i denotes the edge length along the x_i axis of the rectangular parallelepiped. The Lagrangian minimization with a Rayleigh-Ritz approach[11,12] determines the resonance frequencies together with the associated sets of expansion coefficients a^i_k through an eigenvalue problem. According to deformation symmetry about the three principal axes, free-vibration resonance frequencies of an oriented tetragonal

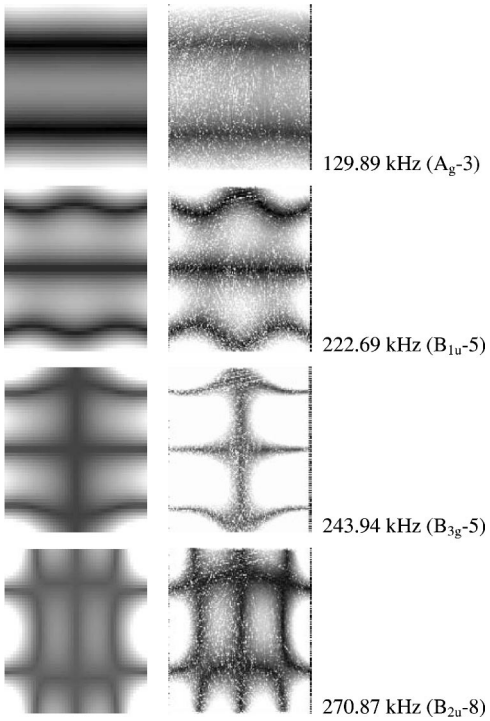

FIG. 2. Calculated (left) and measured (right) distributions of out-of-plane displacement amplitude on the x_1 surface of the specimen. Bright area implies large displacement amplitude and black area zero amplitude, that is, nodal lines. The maximum amplitude is about 1 nm.

rectangular parallelepiped can be divided into eight vibration groups[11,12,18] and, by calculating the resonance frequencies of each vibration group independently, we can reduce the number of basis functions and then the computation time.

Following Ohno's study, we performed a least-squares-fitting procedure for the calculated and measured resonance frequencies to deduce the C_{ijkl} and e_{ijk} simultaneously. In this inverse calculation, comparison of the measurements with the calculations must be made on exactly the same resonance mode. Otherwise, resultant material coefficients are physically meaningless. We achieved correct mode identification by computing the displacement distributions on a vibrating specimen surface using Eq. (6) and comparing them with the measurements (see Fig. 2).[19,20]

The dielectric coefficients ε_{ij} can be determined by capacitance measurements with good accuracy, and we fixed the ε_{ij} at averaged values from previous studies as $\varepsilon_{11}=201.0\times10^{-12}$ and $\varepsilon_{33}=218.7\times10^{-12}$ F/m^2.

A similar analysis as that used in deducing C_{ijkl} and e_{ijk} applies to determination of the independent internal-friction components Q^{-1}_{ijlk} from the peak widths.[13,20,21] A complete set of C_{ijkl} and Q^{-1}_{ijlk} enables one to calculate mechanical losses of all possible ultrasonic modes, including unmeasurable modes, and then to find a less-lossy mode, propagation direction, and surface orientation for designing acoustic devices.

IV. RESULTS

Figure 2 compares some of distributions of the displacement amplitude measured by Doppler interferometry with those calculated by Eq. (6). Excellent agreement allowed us to make unambiguous mode identification. Because such a displacement distribution is hardly affected by the material coefficients and it is governed by shape and orientation of the solid, we do not require *good* initial guesses of C_{ijkl} and e_{ijk} for the inverse calculation. We achieved correct mode identification even with sets of initial guesses different from true values by more than 50%. Thus, we identified 48 peaks and entered them into the inverse calculation. (A few modes gave ambiguous displacement figures because of peak overlapping and low peak heights, which we omitted in the calculation.) Table I shows the measured and calculated resonance frequencies. Their rms difference was 0.27%. Table II shows the elastic constants and piezoelectric coefficient determined in the present study together with those reported previously.

Figure 3 shows internal frictions at individual resonances. Internal friction measured in vacuum is smaller than that in ambient pressure by a factor about 1.5. Energy leakage into air causes background energy loss and increases the as-measured internal friction. Thus Fig. 3 emphasizes the necessity of the internal-friction measurement in vacuum for low-Q^{-1} materials.

In deducing the internal-friction tensor, we assumed it to be independent of frequency. However, in the low-frequency region, internal friction apparently depends on frequency. Thus, we omitted measurements at low frequencies and used five sets of frequency ranges: (i) 50 internal frictions in 150–287 kHz, (ii) 45 in 166–287 kHz, (iii) 40 in 181–287 kHz, (iv) 35 in 204–287 kHz, and (v) 30 in 216–287 kHz. The five sets of internal-friction data yielded identical components of the internal-friction tensor within acceptable error bands. The results are shown in Table II.

V. DISCUSSION

A. Accuracy of the results

First, we discuss the accuracy of our results. This is an important task in the physical point of view because we can discuss physics based on accurate and reliable measurements. Four error sources could affect the resulting coefficients in the present method. They are (i) measurement error for resonance frequencies ($<0.01\%$), (ii) measurement errors for dimensions and density ($<0.02\%$), (iii) misorientation error (less than 0.2°), and (iv) errors in the calculated resonance frequencies ($\sim0.1\%$). Thus, the calculation error dominates the accuracy of the resulting coefficients. It occurs because of the approximation of displacements and electric potential by a linear combination of Legendre polynomials [Eqs. (6)–(8)]. Increasing the number of the basis function reduces this error, but increases the computation time. (We used 60–80 basis functions for a displacement and electric potential in calculating frequencies of one vibration group.) Such a material coefficient that shows contributions to the resonance frequencies smaller than the calculation errors can not be determined accurately. We calculated the contributions of individual coefficients[12] and estimated possible maximum errors using the calculation errors,[20] which are shown in Table II.

TABLE I. Resonance frequencies (MHz) of α-TeO_2 rectangular parallelepiped crystal measured (f_{meas}) by the piezoelectric tripod at 30 °C and calculated (f_{calc}) by the Lagrangian minimization method. The rms difference is 0.27%. Mode notation follows Mochizuki (Ref. 18).

Mode	f_{meas}	f_{calc}	diff. (%)
Au-1	0.102052	0.101939	−0.11
Au-2	0.153248	0.153415	0.11
Au-3	0.183265	0.182991	−0.15
Au-4	0.184328	0.184025	−0.16
Au-5	0.245183	0.245234	0.02
Ag-1	0.063715	0.06356	−0.24
Ag-2	0.085905	0.0855	−0.47
Ag-3	0.129891	0.129813	−0.06
Ag-4	0.190581	0.190765	0.1
Ag-5	0.208573	0.208927	0.17
Ag-6	0.211971	0.212273	0.14
Ag-7	0.214433	0.214899	0.22
Ag-8	0.238184	0.237626	−0.23
B1u-1	0.063552	0.063368	−0.29
B1u-2	0.134526	0.134383	−0.11
B1u-3	0.210471	0.210603	0.06
B1u-4	0.215879	0.21501	−0.4
B1u-5	0.22269	0.222743	0.02
B1u-6	0.239386	0.239906	0.22
B2u-1	0.077949	0.077734	−0.28
B2u-2	0.13616	0.135926	−0.17
B2u-3	0.156802	0.156779	−0.01
B2u-4	0.180404	0.180469	0.04
B2u-5	0.204789	0.204603	−0.09
B2u-6		0.232348	
B2u-7	0.254821	0.257404	1.01
B2u-8	0.270873	0.271265	0.14
B3u-1	0.075063	0.074816	−0.33
B3u-2	0.14183	0.141669	−0.11
B3u-3	0.156986	0.156933	−0.03
B3u-4		0.181832	
B3u-5	0.196158	0.195894	−0.13
B3u-6	0.232394	0.232556	0.07
B3u-7	0.266271	0.268832	0.96
B3u-8	0.273315	0.273779	0.17
B1g-1	0.127168	0.127106	−0.05
B1g-2	0.150752	0.150416	−0.22
B1g-3	0.169746	0.169433	−0.18
B1g-4		0.243256	
B1g-5	0.250712	0.250676	−0.01
B1g-6	0.25806	0.259008	0.37
B1g-7		0.260292	
B1g-8	0.272143	0.272042	−0.04
B2g-1	0.108169	0.108011	−0.15
B2g-2		0.166158	
B2g-3	0.176056	0.176235	0.1
B2g-4	0.220302	0.220517	0.1
B2g-5	0.245582	0.246129	0.22
B3g-1	0.106792	0.106619	−0.16
B3g-2	0.163709	0.163706	0
B3g-3	0.172693	0.172852	0.09
B3g-4	0.226291	0.226663	0.16
B3g-5	0.243943	0.244581	0.26

Our elastic constants are consistent with those measured previously by conventional methods with larger errors. However, our piezoelectric coefficient e_{14} is remarkably larger than that measured by Ohmachi and Uchida[5] by 53%. This difference far exceeds the error limit. We consider our value more reliable because the previous measurement involved many error sources associated with the use of different crystals, combination of different measurement methods, use of electrodes and coupling materials for the acoustic transduction. The present method excludes all these error sources.

B. Elastic constants: Crystal physics

We discuss the interrelationships among crystal structure, elastic constants, and interatomic bonding. Paratellurite shows the following remarkable elastic properties.

(i) Longitudinal modulus C_{33} exceeds C_{11} by a factor 2. The crystal is much stiffer along the x_3 axis.

(ii) This stiffness anisotropy appears especially in $E_{\langle 001\rangle}$ exceeding $E_{\langle 100\rangle}$ by a factor 11. $E_{\langle 001\rangle}$ and $E_{\langle 100\rangle}$ denote Young's moduli along the x_3 and x_1 directions, respectively.

(iii) The diagonal shear modulus $C'=(C_{11}-C_{12})/2$ is very small. Note that $C_{66}/C'=28$, an enormous shear anisotropy.

(iv) The in-plane Poisson ratio ν_{12} is almost unity, while the out-of-plane Poisson ratio ν_{13} is almost zero.

(v) The longitudinal modulus $C^L_{\langle 110\rangle}=(C_{11}+C_{12}+2C_{66})/2$ exceeds C_{33}. $C^L_{\langle 110\rangle}$ denotes C_{11} in a coordinate system where the x_1 and x_2 axes are rotated about the x_3 axis by 45°.

(vi) Poisson ratio $\nu_{\langle 110\rangle\langle \bar{1}10\rangle}$ is negative. $\nu_{\langle 110\rangle\langle \bar{1}10\rangle}$ denotes Poisson ratio ν_{12} in the coordinate system rotated about the x_3 axis by 45°. Negative Poisson ratios (transverse expansion during uniaxial extension) signal odd behavior, often related to an internal degree of freedom.

We identify two principal reasons for these remarkable elastic properties. First is bond strength for stretching of atomic pairs. Figure 4 shows the unit cell containing four formula units, or twelve atoms. This cell follows from Thomas's crystal-structure determination.[22] Both oxygen and tellurium occur in column VIB of Mendeleev's table. Usually, we call such elements isoelectronic. Oxygen, with electron configuration $[\mathrm{He}]2s^2 2p^4$, almost always shows a -2 valence (two electrons required to complete an octet). Tellurium, with electron configuration $[\mathrm{Kr}]4d^{10}5s^2 5p^4$, can also show a -2 valence. But, as a cation it shows valence $+6$ or

TABLE II. Elastic constants C_{ij} (GPa), piezoelectric coefficient e_{14} (C/m^2), Poisson ratio ν_{ij}, and internal friction Q_{ij}^{-1}, of α-TeO_2 at 30 °C.

	Present	Ohmachi and Uchida (Ref. 5)	Arlt and Schweppe (Ref. 4)	Mirgorodsky *et al.* (Ref. 7)[a]	Q_{ij}^{-1} (10^{-5})
C_{11}	55.75±0.02	55.7	56.0	59.3	6.0±0.6
C_{33}	106.6±1.5	105.8	105.1	102.2	5.8±1.7
C_{44}	26.6±0.2	26.5	27	12.3	7.7±0.9
C_{66}	65.8±0.3	65.9	66.8	43.6	12.8±0.4
C_{12}	51.1±0.1	51.2	51.6	53.8	5.9±0.7
C_{13}	22.9±0.9	21.8	27.2	53.4	0.1±0.9
e_{14}	0.330±0.03	0.216			
B	45.3				4.6
C'	2.32				7.4
$C^L_{\langle 110\rangle}$	119.3				9.7
$E_{\langle 100\rangle}$	8.87				
$E_{\langle 001\rangle}$	96.8				
ν_{12}	0.91				
ν_{13}	0.019				
ν_{31}	0.21				
$\nu_{\langle 110\rangle\langle \bar{1}10\rangle}$	−0.15				
$\nu_{\langle 110\rangle\langle 001\rangle}$	0.25				
$\nu_{\langle 001\rangle\langle 110\rangle}$	0.21				

[a]Calculated by a joint model.

+4. In TeO_2, the latter valence occurs, meaning that the 2 electrons comprise an inert pair, a nonbonding valence-electron pair.

We must consider three bond types: Te-Te, O-O, and Te-O. The closest Te-Te distance (d) in metallic tellurium is 2.86 Å. In TeO_2, the closest Te-Te distance is 3.74 Å. Because interatomic interactions go as d^{-n} (n ranges from 2 to 10 or higher), we expect little Te-Te contribution to bonding. The shortest O-O bond in TeO_2 measures 2.69 Å. This compares with a Shannon-Prewitt[23] fourfold-coordination value of 2.48 Å. Thus, we expect some O-O contribution to bonding. In Fig. 4, the shortest bonds are represented by bonds between the 5-6, 10-12, 7-8, 9-11 oxygen-atom pairs.

As for the Te-O bonds, we note first that in the free Te-O molecule the bond length is 1.83 Å, the bond angle being unknown.[24] (In SeO_2, the bond angle equals 114°.[25]) Adding the Te, O covalent radii (0.73, 1.35 Å) gives for the solid a predicted bond length of 2.08 Å. Figure 4 shows Te-O bonds of 1.88 Å, typifying strong covalent low-coordination bonds (between pairs 1-5, 2-6, 2-10, 3-7, 3-12, 4-8, 4-9 in the diagram). Te-O bonds also occur with larger than optimum distance: 2.12 Å (atom pairs 2-5, 2-12, 4-7, 4-11 in the diagram). Because of their extra length (13%) these bonds are much weaker. Thus, as emphasized by Mirgorodsky and coauthors,[7] TeO_2 consists essentially of TeO_4 units, with two strong Te-O bonds and two weak Te-O bonds. The crystal builds up by a string of Te-O bonds alternating two-strong/two-weak/two-strong. The crystallographic arrangement of

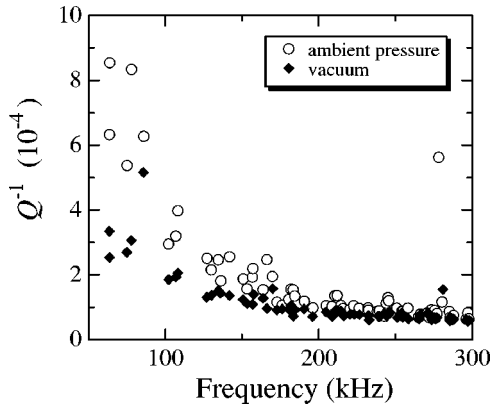

FIG. 3. Internal friction versus frequency measured in vacuum and ambient pressure at 30 °C.

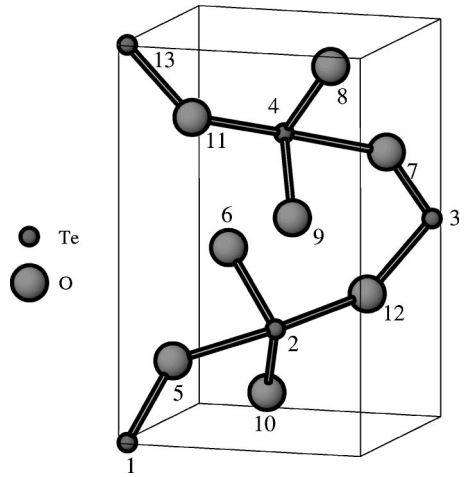

FIG. 4. Crystallographic structure in a unit cell of paratellurite.

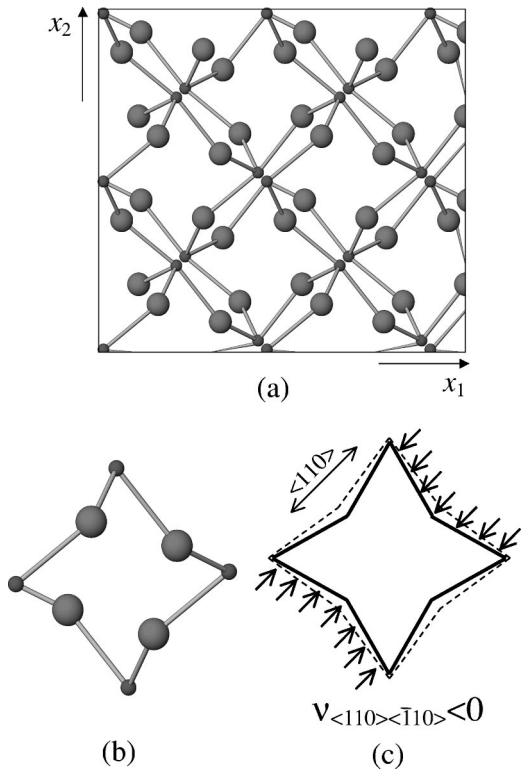

FIG. 5. (a) Lattice projection on the x_1-x_2 plane of paratellurite, (b) star-shape truss unit constructing the lattice structure, and (c) a schematic explanation of a negative Poisson ratio when the stat-shape truss is deformed along the ⟨110⟩ direction (dashed line indicates the truss shape before the deformation).

these strong, weak bonds explains some of TeO_2's elastic properties.

This crystal physics explains observations (i) and (ii), because the strong bonds nearly align with the x_3 axis while the weak bonds align close to the x_1-x_2 plane [see Fig. 5(a)]. However, it is less satisfactory in explaining observations (iii)–(v), especially observation (v), where it predicts $C^L_{\langle 110\rangle} < C_{33}$ because a projection onto the basal plane shows that the weak bond aligns well with either [110] or $[\bar{1}10]$.

As a second part of the crystal physics, we consider a star-shape truss structure. We see that the lattice structure projected onto the basal plane [Fig. 5(a)] consists of a star-shape unit composed of four Te atoms and four oxygen atoms as shown in Fig. 5(b): Te and O atoms connect with weak and strong bonding alternately. The unit structure behaves as a truss structure when the resistance for bending of Te-O bonds is weak. It is well known that a square truss, consisting of four rigid bars connected to each other by free-rotation joints, shows no resistance to a shear deformation along the square's side (corresponding to $C' \cong 0$) and that Poisson ratio nearly equals unity when it is deformed along a direction inclined by 45° from the side. These properties apply to the star-shape truss structure. Furthermore, the star-shape truss yields a negative Poisson ratio when deformed along a direction perpendicular to the sides as shown in Fig. 5(c). Thus, by considering the star-shape truss structure on the x_1-x_2 basal plane as well, we can explain all of the observations (i)–(vi), that is, large elastic anisotropies in the basal-plane and x_3 directions (large C_{33}/C_{11} and $E_{\langle 001\rangle}/E_{\langle 100\rangle}$), unusual Poisson ratios ($\nu_{12} \approx 1, \nu_{13} \approx 0, \nu_{\langle 110\rangle\langle \bar{1}10\rangle} < 0$), nearly zero shear modulus C', and the large modulus $C^L_{\langle 110\rangle}$, which reflects the bond strength for stretching.

The bulk modulus B is low, 45 GPa. Here, independent of the shear-mode C_{ijkl},[26]

$$B = \frac{1}{9} C_{iijj} \quad [\text{sum on } i,j]. \tag{9}$$

It is useful to consider the linear compressibilities

$$\kappa = s_{ijkl} \ell_i \ell_j . \tag{10}$$

Here s_{ijkl} denotes the tensor inverse of C_{ijkl} and ℓ denotes components of a unit vector. For tetragonal symmetry, this becomes

$$\kappa = (s_{11}+s_{12}+s_{13}) - (s_{11}+s_{12}-s_{13}-s_{33})\ell_3^2. \tag{11}$$

Substitution gives $\kappa(100) = 0.0081\ \text{GPa}^{-1}$ and $\kappa(001) = 0.0059\ \text{GPa}^{-1}$. In this property, TeO_2 shows near isotropy. The bulk modulus relates to these by

$$B = (2\kappa(100) + \kappa(001))^{-1}. \tag{12}$$

Thus the low bulk modulus reflects the high compressibility in the basal plane.

Acoustically, the Debye temperature Θ_D is defined as[27]

$$\Theta_D = \frac{h}{k}\left(\frac{3N}{4\pi}\right)^{1/3}\left(\frac{\rho}{\mu}\right)^{1/3} \nu_m . \tag{13}$$

Here, k denotes Boltzmann constant, h Planck constant, N Avogadro constant, and μ the mean atomic mass. ν_m denotes the mean sound velocity given by

$$\frac{3}{\nu_m^3} = \frac{2}{\nu_S^3} + \frac{1}{\nu_L^3}. \tag{14}$$

Here ν_S and ν_L denote the average-over-direction shear-wave and longitudinal-wave velocities, respectively. We numerically determined ν_m using the monocrystal C_{ij} to solve the Christoffel equation for a large number of random directions and integrating the mean sound velocity over all space.[28] This method yields $\nu_m = 1907$ m/s and $\Theta_D = 231.9$ K at 30 °C. This value is much smaller than for usual oxide crystals ($\Theta_D = 781$ K at room temperature for TiO_2, for example),[27] reflecting low average shear-wave velocity. It agrees well with the heat-capacity value.[29]

C. Internal friction

We consider phonon-phonon interactions as the principal origin of paratellurite's internal friction. Through lattice anharmonicity, acoustic waves break the equilibrium state of thermal phonons. Scattered phonons subsequently equilibrate by interacting with a low-frequency-mode acoustic phonon and other thermal-mode phonons, during which an energy loss occurs. The energy loss relates closely with a dimen-

sionless constant, the Grüneisen parameter γ, which shows the degree of a crystal's anharmonicity and quantifies relationships between solid-state thermal and elastic properties. According to the Akhieser result,[30] the energy loss is proportional to γ^2 as

$$Q^{-1}_{phonon}=\frac{C_p T\gamma^2}{\rho\nu^2}\frac{\omega\tau}{1+\omega^2\tau^2}. \quad (15)$$

Here, C_p denotes specific heat per unit volume, T absolute temperature, and ν sound velocity. τ denotes the relaxation time, the time required to equilibrate the interchange of acoustic energy with thermal energy. Equation (15) is valid when $\omega\tau<1$, which normally applies to measurements at room temperature at kilohertz frequencies.

On the other hand, Ledbetter[31] showed that the temperature derivative of the bulk modulus B relates simply to the Grüneisen parameter γ:

$$\left(\frac{dB_S}{dT}\right)_P=-\frac{3k\gamma(\gamma+1)}{V_a}. \quad (16)$$

Here, V_a denotes the atomic volume. A relationship like Eq. (16) should hold for other C_{ijkl}. Thus the magnitude of temperature derivative of C_{ijkl} and internal friction Q^{-1}_{ijlk} should show a positive correlation through the Grüneisen parameter when phonon-phonon interactions provide the dominant damping mechanism. Indeed, we see their positive correlation in Fig. 6.

Above discussion applies considering the magnitude of internal friction at a constant frequency. However, concerning the frequency dependence of internal friction, our result fails to obey the conventional phonon-phonon theory because the theory predicts an increase of internal friction with increasing frequency. Recent studies on internal friction in piezoelectric crystals show that internal friction is independent of frequency[20] or decreases with increasing frequency.[32] Thus the frequency-dependence term in the phonon-phonon interaction theory may need to be improved.

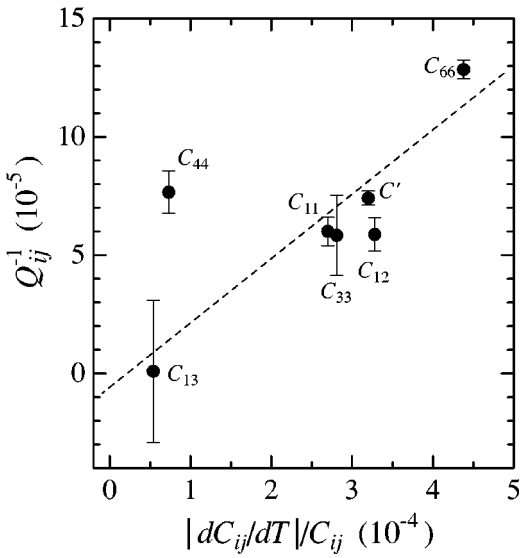

FIG. 6. Correlation between internal-friction components and magnitudes of normalized temperature derivatives of elastic constants. The temperature derivative values are taken from Ohmachi and Uchida (Ref. 5).

VI. CONCLUSIONS

(1) We simultaneously determined all the elastic constants, corresponding internal frictions, and piezoelectric coefficient of paratellurite (α-TeO_2) by an original RUS/laser hybrid method. Our elastic coefficients are consistent with those reported previously, but our piezoelectric coefficient is larger than the previous value by 53%.

(2) Paratellurite shows remarkable elastic properties, including a negative Poisson ratio, very strong anisotropy between Young's moduli $E_{\langle 100\rangle}$ and $E_{\langle 001\rangle}$, and almost zero value of diagonal-shear C'. All these properties can be understood by considering alternating weak-strong Te-O bonds and a star-shape truss structure on the basal plane. The latter indicates very weak resistance for Te-O-bond bending.

(3) The elastic Debye temperature $\Theta_D=232$ K at ambient temperature agrees well with the heat-capacity value. For oxides, it is especially low.

(4) Internal friction correlates with the elastic-constant temperature derivatives. This correlation is interpreted as meaning that Q^{-1} arises from phonon-phonon interactions.

ACKNOWLEDGMENT

To draw the unit cell, we used the commercial software ATOMS.

[1] R. W. Dixon and M. G. Cohen, Appl. Phys. Lett. **8**, 205 (1966).
[2] V. B. Voloshinov and V. Ya. Molchanov, Opt. Laser Technol. **27**, 307 (1995).
[3] N. Uchida and Y. Ohmachi, J. Appl. Phys. **40**, 4692 (1969).
[4] G. Arlt and H. Schweppe, Solid State Commun. **6**, 783 (1968).
[5] Y. Ohmachi and N. Uchida, J. Appl. Phys. **41**, 2307 (1970).
[6] P. S. Peercy, I. J. Fritz, and G. A. Samara, J. Phys. Chem. Solids **36**, 1105 (1975).
[7] A. P. Mirgorodsky, T. Merle-Méjean, J.-C. Champarnaud, P. Thomas, and B. Frit, J. Phys. Chem. Solids **61**, 501 (2001).
[8] J. C. Champarnaud-Mesjard, S. Blanchandin, P. Thomas, A. Mirgorodsky, T. Merle-Méjean, and B. Frit, J. Phys. Chem. Solids **61**, 1499 (2001).
[9] *IEEE Standard on Piezoelectricity in IEEE Transactions on Sonics and Ultrasonics*, Vol. SU-31, ANSI/IEEE Std 176-1978 (IEEE, New York, 1979).
[10] R. Smith and F. Welsh, J. Appl. Phys. **42**, 2219 (1971).
[11] I. Ohno, J. Phys. Earth **24**, 355 (1976).
[12] A. Migliori, J. Sarrao, W. Visscher, T. Bell, M. Lei, Z. Fisk, and R. Leisure, Physica B **183**, 1 (1993).
[13] H. Ledbetter, C. Fortunko, and P. Heyliger, J. Mater. Res. **10**, 1352 (1995).

[14] H. Ogi, H. Ledbetter, S. Kim, and M. Hirao, J. Acoust. Soc. Am. **106**, 660 (1999).
[15] H. Ogi, M. Dunn, K. Takashima, and H. Ledbetter, J. Appl. Phys. **87**, 2769 (2000).
[16] J. Schreuer, IEEE Trans. Ultrason. Ferroelectr. Freq. Control **49**, 1474 (2002).
[17] I. Ohno, Phys. Chem. Miner. **17**, 371 (1990).
[18] E. Mochizuki, J. Phys. Earth **35**, 159 (1987).
[19] H. Ogi, K. Sato, T. Asada, and M. Hirao, J. Acoust. Soc. Am. **112**, 2553 (2002).
[20] H. Ogi, N. Nakamura, K. Sato, M. Hirao, and S. Uda, IEEE Trans. Ultrason. Ferroelectr. Freq. Control **50**, 553 (2003).
[21] M. Hirao and H. Ogi, *EMATs for Science and Industry* (Kluwer Academic, Boston, 2003), p. 140.
[22] P. Thomas, J. Phys. C **21**, 4611 (1988).
[23] R. Shannon and C. Prewitt, Acta Crystallogr., Sect. B: Struct. Crystallogr. Cryst. Chem. **B25**, 925 (1969).
[24] R. Shannon, Acta Crystallogr., Sect. A: Cryst. Phys., Diffr., Theor. Gen. Crystallogr. **A32**, 751 (1976).
[25] *Structure Data of Free Polyatomic Molecules*, edited by K. Kuchitsu, Landolt-Börnstein NDFRSC, New Series, Group II, Vol. 25A (Springer, Berlin, 1998).
[26] J. Nye, *Physical Properties of Crystals* (Oxford, London, 1960), pp. 145, 146.
[27] O. L. Anderson, *Equations of State of Solids for Geophysics and Ceramic Science* (Oxford, New York, 1995).
[28] H. Ledbetter and S. Kim, in *Handbook of Elastic Properties of Solids, Liquids, and Gases*, edited by M. Levy, H. Bass, and R. Stern (Academic, New York, 2001), Vol. 2, p. 97.
[29] G. White, S. Collocott, and J. Collins, J. Phys.: Condens. Matter **2**, 7715 (1990).
[30] W. Mason, in *Physical Acoustics*, edited by W. Mason (Academic, New York, 1965), Vol. IIIB, p. 254.
[31] H. Ledbetter, Phys. Status Solidi B **181**, 81 (1994).
[32] W. Johnson, S. Kim, and D. Lauria, *Proc. IEEE/EIA International Frequency Control Symposium* (IEEE, New York, 2000), p. 186.